# Chapter 5

# Io's Escaping Neutrals

## 5.1 Introduction

Observations of Io's extended atmosphere have painted a portrait of a highly dynamic and variable region. The volcanic source processes vary in time, magnitude, and location on Io's surface. Large variations in surface temperature result in the daily collapse of the thin atmosphere. External forces such as Jupiter's rapidly rotating magnetic field and the intense bombardment by plasma torus ions strip the atmosphere away at a rate of a ton per second. Loss of atmospheric neutrals then provides the source regions for the plasma through the formation of Io's corona and extended neutral clouds. Observations of these features provide important insight into the magnitude and variability of this atmospheric loss and the quantity of material available for the formation of the torus. Telescopic observations however are only capable of measuring the line-of-sight integrated column densities and intensities and *in situ* measurements by spacecraft are rare and only measure a single slice through the highly variable plasma. Understanding the details of the escape of Io's atmosphere and the formation of the plasma torus requires a knowledge of the three dimensional distributions of neutrals near Io. This requires a model which can simulate the motions of neutrals to determine probable distributions which can be compared with observations.

Although other authors have published neutral cloud models (e.g. Smyth and Combi (1988a,b)), the development of a new model for understanding Io's neutral fea-

tures is necessary to take advantage of new observations of the neutral clouds and the plasma torus. Recent observations of the Io plasma torus (Schneider and Trauger 1995; Brown 1994) have shown that the intensity and apparent motions of the plasma are extremely variable. In this chapter I describe the neutral cloud model and an empirical treatment of the plasma torus which can reproduce the observed variability in the brightness and morphology of the plasma torus. In chapters 6 and 7 the model is used to investigate in detail the morphologies of Io's corona and extended neutral cloud. The neutral cloud model can also be applied to future studies of Io's neutral features as well as investigations of neutral loss from other solar system objects.

The chapter is organized as follows: In Section 5.2 I discuss the previously published model of Smyth and Combi (1988a,b) with which I will compare the current model. Differences between the two models are discussed in Section 5.3 which is devoted to describing the model in detail. In addition to a description of the approach taken to determine the spatial distribution of neutrals within $\sim$ 10 $R_J$ of Jupiter, I describe the flux distributions of atoms ejected from Io's exobase and my treatment of the plasma torus which governs neutral loss. I have developed a framework for using observations of plasma torus variability to determine the spatially and temporally varying plasma properties. I use this framework to determine characteristics of the lifetime of neutrals as a function of the local time, magnetic longitude, and distance from Jupiter. The chapter concludes in Section 5.4 with several applications of the model to demonstrate that the earliest observations of the sodium neutral cloud can be simulated with this model.

In the following chapters I discuss in detail the comparison between observations reported in this thesis and modeling results of the corona (Chapter 6) and the extended neutral cloud (Chapter 7).

## 5.2 Previous Neutral Cloud Models

Modeling efforts to understand Io's sodium emission began almost immediately after its discovery. These models are reviewed in Chapter 1. Included here is a description of the model introduced by Smyth and Combi (1988a) as a general model for Io's neutral clouds. This work has continued most recently with several studies of Io's oxygen emissions (Smyth and Marconi 2000; Oliversen et al. 2001).

Smyth and Combi (1988a) developed the framework for a sophisticated neutral cloud model based upon "the conservation in phase space of the one-particle distribution function $f(\mathbf{v}, \mathbf{x}, t)$ for a gas species." This generalized model was applied to the sodium cloud in a followup paper (Smyth and Combi 1988b). The goals of this study were to explain the physical origin of the predominately forward sodium cloud and the east/west brightness asymmetry in the near Io cloud (Bergstralh et al. 1977). They found that each of these questions could be explained as a consequence of sodium atoms sputtered isotropically from Io's exobase into the radially non-uniform plasma torus. The structure of the torus results in a longer sodium lifetime for atoms which move interior to Io's orbit, which form the leading cloud, than for atoms which move exterior to Io's orbit forming the trailing cloud. The flux distribution from the exobase needed to reproduce adequately the east/west asymmetry was either a classical sputtering flux distribution ($\alpha = 3$ in Equation 2.12) or a Thomas-Fermi-like incomplete collisional cascade sputtering flux distribution ($\alpha = 7/3$); they preferred the latter because of the increased flux of high speed (12–25 km $s^{-1}$) neutrals which they hypothesized populate the fast sodium directional feature. The work of Wilson and Schneider (1999) and that presented in Chapter 4 show that the sodium directional feature is created through a different mechanism than the slow sodium cloud. Therefore the preference for $\alpha = 7/3$ is not necessary.

Smyth and Combi also introduced a parameterization of the plasma torus in

their second paper which is used in their later work. In the discussion which follows in the this chapter, I compare their treatment of the plasma torus with that I have developed. Although most of the differences between the two methods stem from recent observational results which I have used, I also use a different physical description of the orientation and motions of the plasma torus.

## 5.3 A Model of Io's Neutral Clouds

### 5.3.1 Description of the model

The model described here is an extension of the model of Wilson and Schneider (1999) which has previously been used to describe Io's directional feature (see Chapter 4), the molecular ion stream, and the extended sodium disk that is centered on Jupiter and has a radius of $\sim$ 500 $R_J$. The integration algorithm for determining the motions of neutral atoms, which is the basic core of the model, remains unchanged from Wilson's model. However, because the foci of this thesis are Io's corona and extended neutral cloud, several major changes have been made in regard to the lifetimes of neutral atoms within $\sim$ 8 $R_J$ of Jupiter. First, the description of the plasma torus has been refined to include observed variations in brightness and the effects of the east/west electric field. Second, changes have been made in calculating the lifetimes once the local plasma parameters have been determined. The improvement of the sodium electron impact ionization cross sections (Johnston and Burrow (1995),Chapter 2) resulted in a significant change in the sodium lifetime. I have also included charge exchange cross sections of oxygen and sulfur so that these neutral clouds can be modeled. Lastly, I have rewritten much of the model code so that its run speeds are improved allowing the higher spatial resolution simulations which are needed to understand the features close to Io.

In order to simulate the creation of the neutral clouds and their loss into the

plasma torus, a particle approach is used to follow sodium atoms ejected from Io's exobase. I follow packets representing a number of atoms that are subjected to the forces of Io's gravity, Jupiter's gravity, and solar radiation pressure (for sodium only). Ionization reduces the number of atoms that the packet represents. The coordinate system (Figure 5.1) is fixed such that the z-axis is along Jupiter's north-south axis perpendicular to the equatorial rotational plane where the satellites lie. The y-axis is along the sun-Jupiter line with the positive direction pointing radially away from the sun. The x-axis is oriented perpendicular to the y- and z-axes pointing from Jupiter's east (dawn) side to the west (dusk) side.

The gravitational accelerations that packets experience from both Jupiter and Io are calculated:

$$\mathbf{a_p} = \frac{d^2\mathbf{x}}{dt^2} = -\frac{GM_p}{\mathbf{r_p}^3} \tag{5.1}$$

where p refers to either Jupiter or Io and $r_p$ is the distance from the packet to the object ($r_p = \sqrt{x_p^2 + y_p^2 + z_p^2}$ with $x_p$, $y_p$, and $z_p$ being the differences in the x, y, and z coordinates of the packets and the object p). $M_p$ is the mass of the object and G is the universal gravitational constant.

The acceleration due to radiation pressure, as discussed in Chapter 2, is given by:

$$\mathbf{a_{rad}} = [a_{x,rad}, a_{y,rad}, a_{z,rad}] = [0, 0.580\,(\gamma_1 + 2\gamma_2)\,, 0] \tag{5.2}$$

Because the direction from the sun to Jupiter is defined to be the y-axis, radiation pressure always acts in the positive y direction and the force only has one component. This simplifies the calculation of the radiation acceleration since it depends on the radial velocity of the packet relative to the sun, which is simply the velocity in the y direction; i.e., $\gamma_1$ and $\gamma_2$ are functions of $v_y$ only.

Combining the effects of the three accelerations yields:

$$\mathbf{a} = \mathbf{a_J} + \mathbf{a_{Io}} + \mathbf{a_{rad}} \tag{5.3}$$

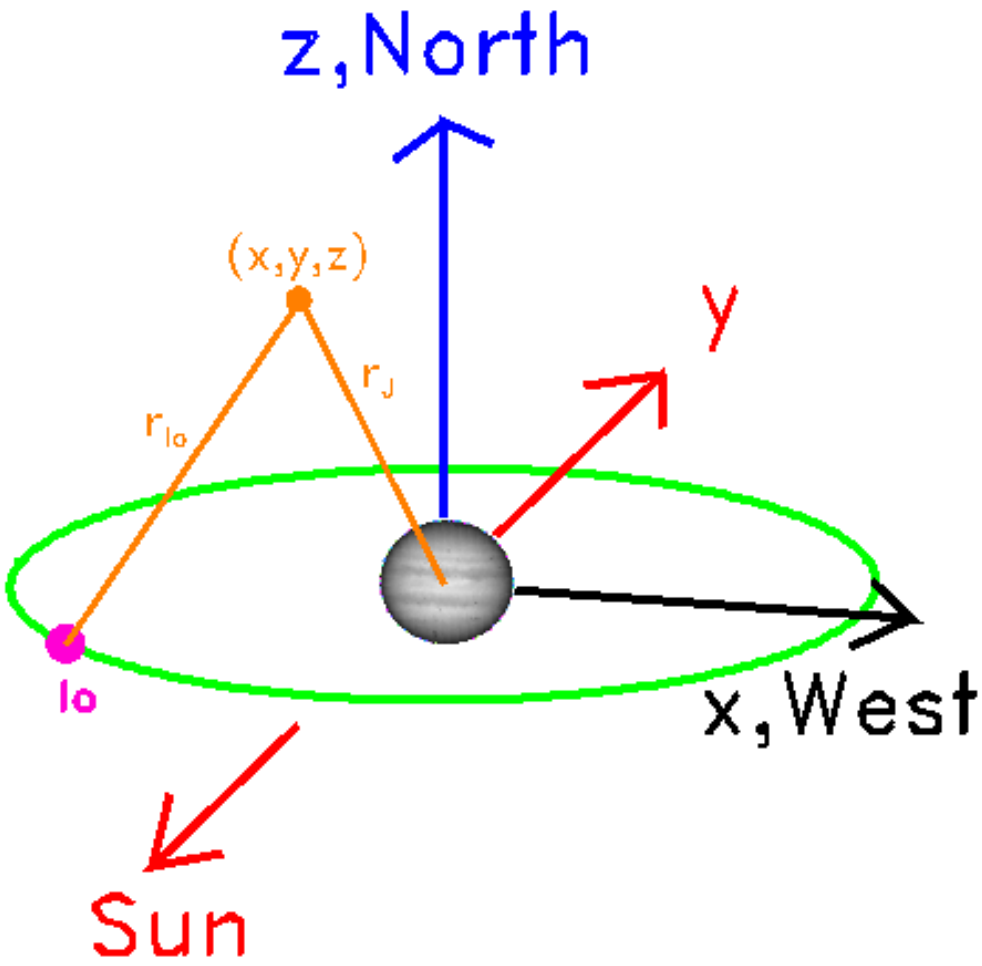


Figure 5.1 Sketch of the coordinate system used in the model. The origin of the coordinate system is fixed at Jupiter's center. The x-axis is direction from east to west. The y-axis is directed radially away from the sun. The z-axis is aligned north along Jupiter's spin axis. Io's orbit is shown in green with Io indicated by the pink dot at orbital phase $\phi = 135°$. A packet is at position (x,y,z) with the distances $r_J$ and $r_{Io}$ labeled.

or

$$\begin{aligned}
\frac{d^2x}{dt^2} &= -\frac{GM_Jx_J}{r_J^3} + -\frac{GM_{Io}x_{Io}}{r_{Io}^3} \\
\frac{d^2y}{dt^2} &= -\frac{GM_Jy_J}{r_J^3} + -\frac{GM_{Io}y_{Io}}{r_{Io}^3} + 0.580\,(\gamma_1 + 2\gamma_2) \\
\frac{d^2z}{dt^2} &= -\frac{GM_Jz_J}{r_J^3} + -\frac{GM_{Io}z_{Io}}{r_{Io}^3}
\end{aligned} \tag{5.4}$$

The vectors $\mathbf{r_J}$ and $\mathbf{r_{Io}}$ are the instantaneous distances and directions from the packet to Jupiter and Io (see Figure 5.1). These vectors change constantly due to the motion of the packet through the coordinate system and the motion of Io in its orbit around Jupiter. Jupiter is fixed at the origin of the coordinate system. The system of second-order differential equations is solved using a 4th order adaptive step-size Runge-Kutta technique. Io's orbital phase is tracked for each packet for each step in the solver to determine correctly the gravitational acceleration experienced by each packet. The initial starting positions and velocities of the packets are randomly chosen based on distributions which are supplied. Unless specified otherwise, the initial positions are isotropically distributed over Io's exobase. The packets also are ejected isotropically into the hemisphere tangent to the surface at the packets' starting locations. The initial velocity distribution depends on the loss mechanism from the exobase as discussed in Chapter 2. The starting times for packets are uniformly distributed between the beginning and ending times of the model run, simulating a continuous source from the exobase. This creates a realistic cloud made up of neutrals of all ages between the start and finish of the simulation. The total simulated time depends on the species and the region being modeled.

### 5.3.2 Treatment of the Io Plasma Torus

The instantaneous rate of loss of atoms from each packet and the intensity of observed oxygen and sulfur emission are determined by the local plasma conditions during each time step. Consequently, it is essential to properly determine the location

of the packets in the plasma torus and to understand the structure and variability of the torus to calculate correctly the ionization rate. I will here describe the treatment of the plasma torus used in the model; the ionization rate is discussed in Chapter 2.

Jupiter's magnetic field is approximated as an offset tilted dipole with: a tilt $\alpha_D = 9.8°$ toward the System-III magnetic longitude $\lambda_0 = 200°$, and an offset distance $\delta_D = 0.12$ $R_J$ toward the magnetic longitude $\lambda_D = 149°$ (Figure 5.2). The centrifugal equator is tilted relative to the equatorial plane by the angle $\alpha_C = \frac{2}{3}\alpha_D = 6.5°$. The plasma torus is aligned along the centrifugal equator parallel to the rotation axis. Therefore the ribbon always appears parallel to the rotation axis and is not perpendicular to the centrifugal equator.

To determine the plasma conditions experienced by a packet, I have developed a transformation to a coordinate system in the rest frame of the plasma torus defined by the coordinates M and $\zeta$ in which the ribbon is held fixed at (M,$\zeta$) = (5.83 $R_J$, 0 $R_J$). M is the modified L-shell developed here based on the Voyager *in situ* Plasma Science (PLS) data (Figure 5.3) (Bagenal 1994) and ground-based observations of the local time and magnetic longitude variation in the ribbon location (Schneider and Trauger 1995) (Figure 5.4a). $\zeta$ is the distance along the magnetic field line through the packet from the packet to the centrifugal equator. M differs from the true L-shell, which is based on the offset tilted dipole, due to: (1) the inferred presence of an east/west electric field across Jupiter's magnetosphere, and (2) the observation that the ribbon is offset from the center of Jupiter by approximately one-half the offset of the dipole field. The mathematical transformation from the observer's coordinates to the torus coordinates is given in Appendix B.

A comparison of Figure 5.3 and Figure 5.4(a) reveals an apparent, previously unrecognized inconsistency regarding the position of the ribbon. In the former, the dusk ribbon is at a distance of 5.7 $R_J$. In the latter, the dusk ribbon oscillates between 5.53 and 5.65 $R_J$, a range which excludes the location observed by Voyager. I have

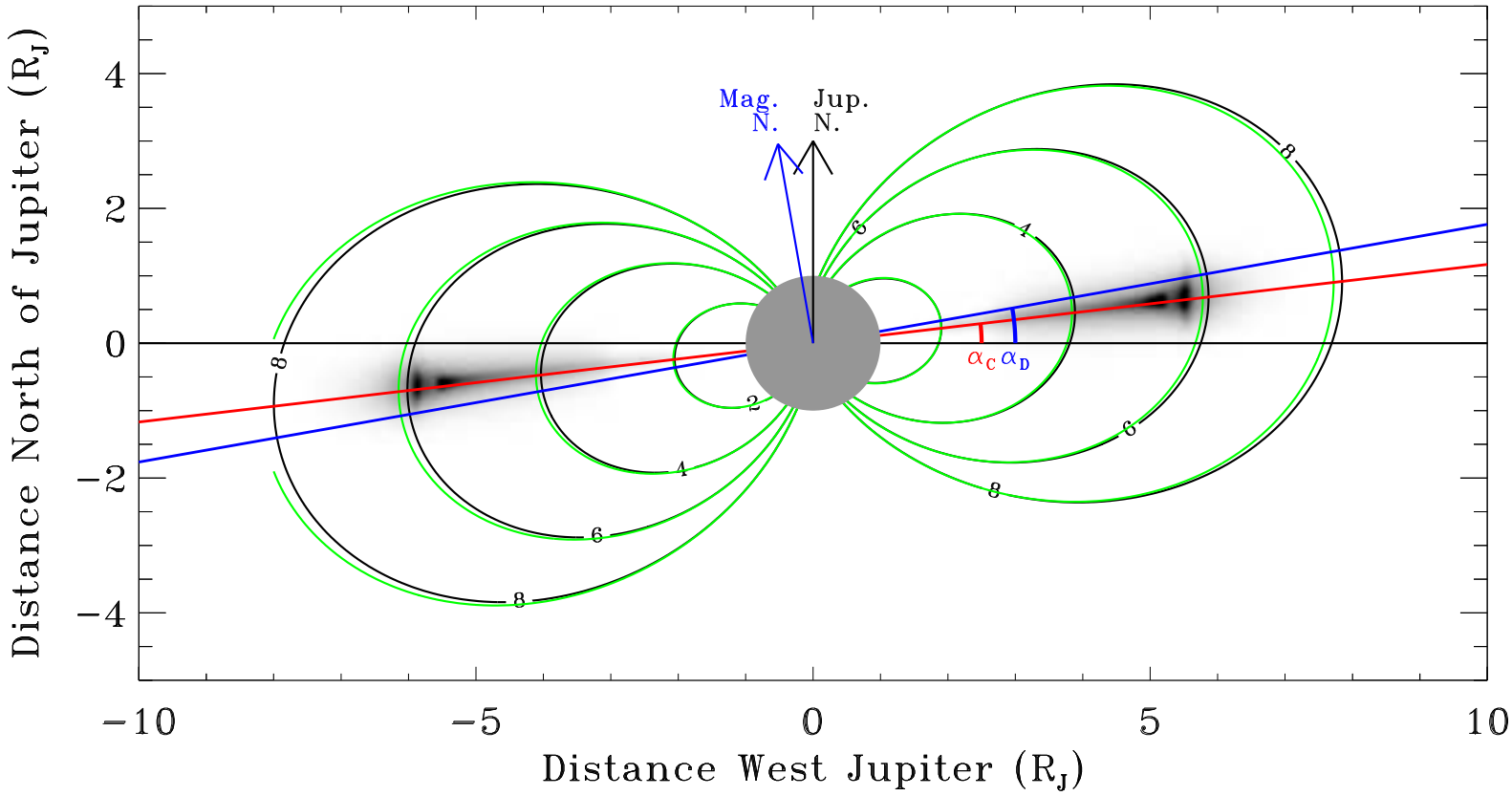


Figure 5.2 Cartoon showing Jupiter's dipole field with the plasma torus aligned along the centrifugal equator. Jupiter's magnetic equator and the direction of magnetic north are shown in blue; the centrifugal equator is shown in red. Jupiter's central meridian longitude ($\lambda_{CML}$) is this depiction is 110°. The L value of the field lines are shown in black. The green contours are the modified L-shell, M, used to determine the plasma parameters.

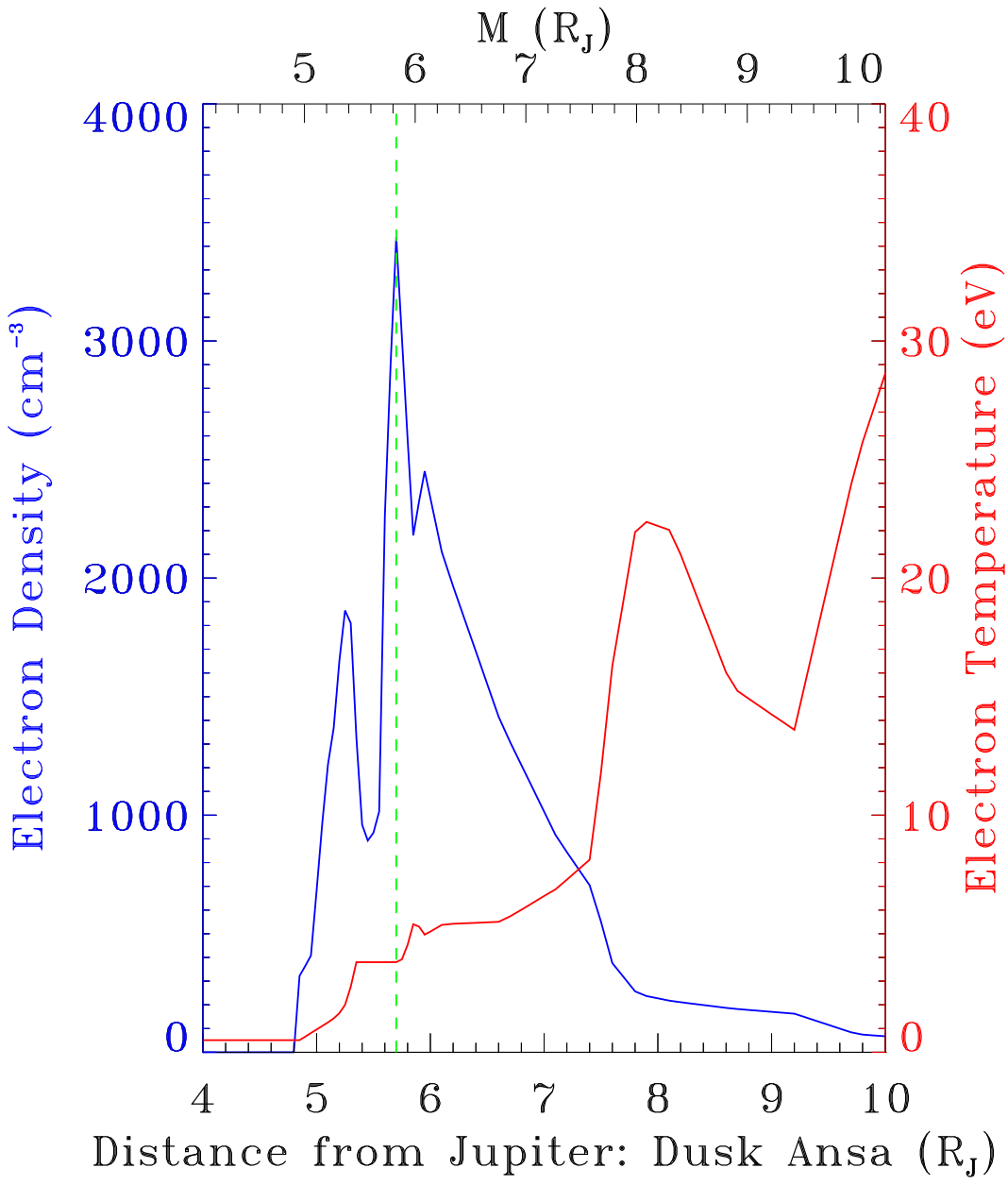


Figure 5.3 The electron density (blue) and temperature (red) in the centrifugal equator measured by the Voyager spacecrafts (Bagenal 1994) are shown as a function of the distance from Jupiter (bottom axis) and the torus M coordinate (top axis) discussed in the text. The broken green line indicates the ribbon observed by Voyager 5.7 $R_J$ from Jupiter and fixed in this coordinate system at M=5.83 $R_J$.

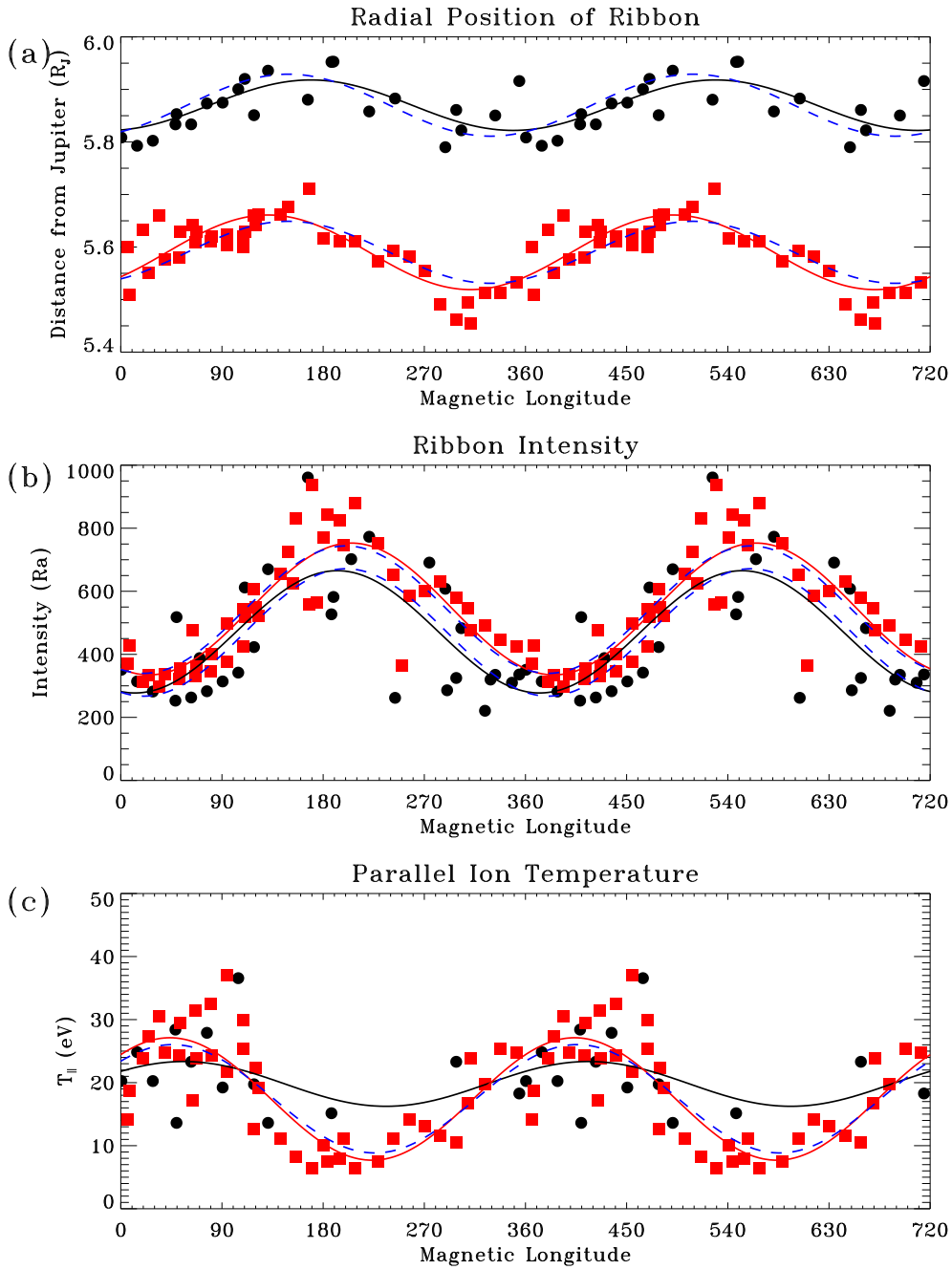


Figure 5.4 Variations in ribbon location, electron density, and parallel ion temperature from observations by Schneider and Trauger (1995). (a) Radial distance of the ribbon from the center of Jupiter as a function of the magnetic longitude of the ansa. Black dots are data from the dawn (eastern) ansa; red squares are from the dusk (western) ansa. The solid black and red lines are fits to the dawn and dusk ansae, respectively. The broken lines show a single sinusoid fit to both ansae. (b) Intensity vs. magnetic longitude. The intensity is proportional to the product of electron density and ion density. Colors as for part (a). (c) $T_{\|}$ vs. magnetic longitude. Temperatures are from the modeling by Schneider et al. (1997) based on the observations of Schneider and Trauger (1995). Colors as for part (a).

found that these two data sets do in fact paint a consistent picture. The resolution to the conflict lies in the difference between *in situ* and remote observing. Voyager measured a slice through the three-dimensional plasma. The ground-based observations detect the total integrated flux along the sight line. When line-of-sight effects are taken into account, the Voyager and ground-based data agree. Figure 5.5 shows a simulated image of the plasma torus and the electron density in Jupiter's east/west plane. The maximum electron density, shown by the broken blue lines, on dawn (dusk) side occurs at 6.02 $R_J$ (5.64 $R_J$). The brightest points in the ribbon (broken red lines), however, are 5.92 $R_J$ at the dawn ansa and 5.56 $R_J$ at the dusk ansa, well inside the distance of maximum electron density and proving that the Voyager and ground-based data are in fact consistent. (The dusk ansa ribbon is not at precisely 5.7 $R_J$ due to the fact that the ribbon moves in and out with an amplitude of $\sim$ 0.06 $R_J$ and depends on magnetic longitude; the central meridian longitude.) Contours of electron density in the centrifugal plane are plotted over the image in green.

The simulated torus images are created by determining the volume emission rate in a grid centered on Jupiter. The plasma electron and ion temperatures and densities are determined by transformation into the plasma coordinate system. The volume emission is then given by:

$$\rho(x, y, z \rightarrow M, \zeta, \phi, \lambda) = C_k(n_e, t_e) n_e(M, \zeta, \phi, \lambda) n_i(M, \zeta, \phi, \lambda) \tag{5.5}$$

in units of photons $cm^{-3}$ $s^{-1}$. $C_k$ is the emission rate coefficient from the CHIANTI atomic physics database (Dere et al. 1997). The volume emission rate is summed along the line-of-sight to determine the observed emission in photons $cm^{-2}$ $s^{-1}$. The dependence of the plasma densities and temperatures on local time $\phi$ and magnetic longitude $\lambda$ is discussed below.

The effect the east/west electric field has is to shift the ribbon east by 0.14 $R_J$; the amount of shift is proportional to the distance from Jupiter, $\Delta R = \epsilon R_0$ (Barbosa

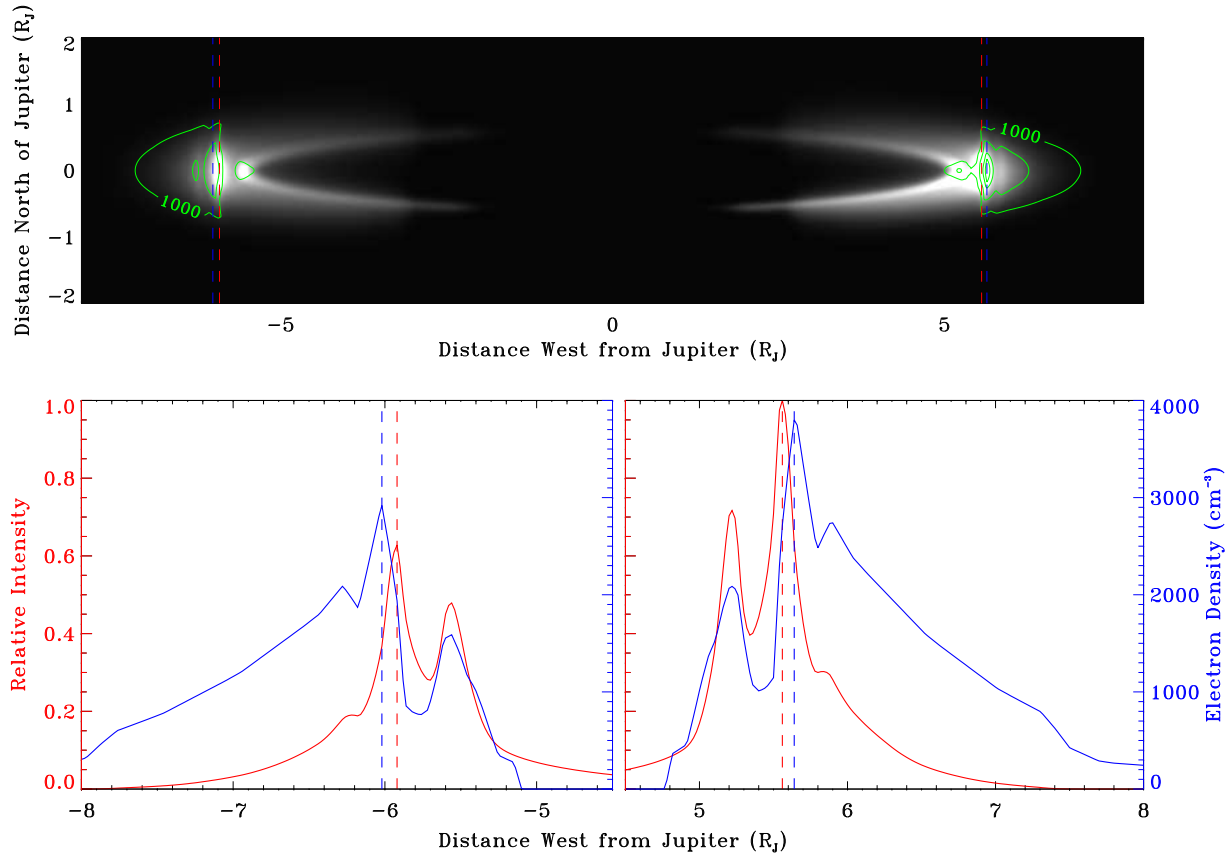


Figure 5.5 Illustration of the importance of line-of-sight effects on Earth-based observations of the plasma torus. (a) A simulated image of singly ionized sulfur. (b) Brightness of the torus (red) and electron density (blue) in the centrifugal plane for the images in (a). The central meridian longitude for this image is $\lambda_{CML} = 20°$.

and Kivelson 1983), where $\epsilon$ is the ratio of the inferred east/west electric field to the corotation electric field. The value of $\epsilon$ which causes a 0.14 $R_J$ shift at the distance of the ribbon (5.83 $R_J$) is 0.024. This measured result based on the ground-based observations is consistent with the assumed value used by Smyth and Combi (1988b). The ground-based observations show that the average observed location of the maximum ribbon brightness is 5.87 $R_J$ at the dawn ansa and 5.59 $R_J$ at the dusk ansa. The average distance for all local times is 5.73 $R_J$. This effect can be simulated with a torus electron profile where the ribbon is at an average distance from Jupiter of 5.83 $R_J$, shifted 0.14 $R_J$ to the east such that the average observed position of the ribbon as a function of local time can be expressed as $5.83 + 0.14 \sin(\phi)$ where $\phi$ is the local time (heliocentric orbital phase). The location of the ribbon (i.e., the position of the maximum electron density at a given orbital phase) is fixed in the plasma coordinate system at $(M, \zeta) = (5.83 R_J, 0 R_J)$.

The local plasma conditions present for each packet depend on the location in the torus (i.e. M and $\zeta$), the local time $\phi$ and magnetic longitude $\lambda$ of the packet. All modulations to the radial plasma profile in the torus start from the Voyager PLS data shown in Figure 5.3. These conditions are assumed the average torus at the dusk ansa. Figure 5.6 shows the values of M and $\zeta$ as functions of Io's magnetic and orbital longitudes. The variation in these coordinates is indicative of the changing plasma environment at Io. Io is inside the ribbon, demarcated by the broken yellow circle, near eastern elongation when crossing the centrifugal equator.

Based on observations (Schneider and Trauger 1995; Brown 1994) and modeling (Bagenal 1994; Schneider et al. 1997; Barbosa and Kivelson 1983; Ip and Goertz 1983)), I have implemented three types of modulation into the description of the plasma torus:

(1) Local Time Variations: Barbosa and Kivelson (1983) and Smyth and Combi (1988b) discuss the effects of the global east/west electric field on the plasma

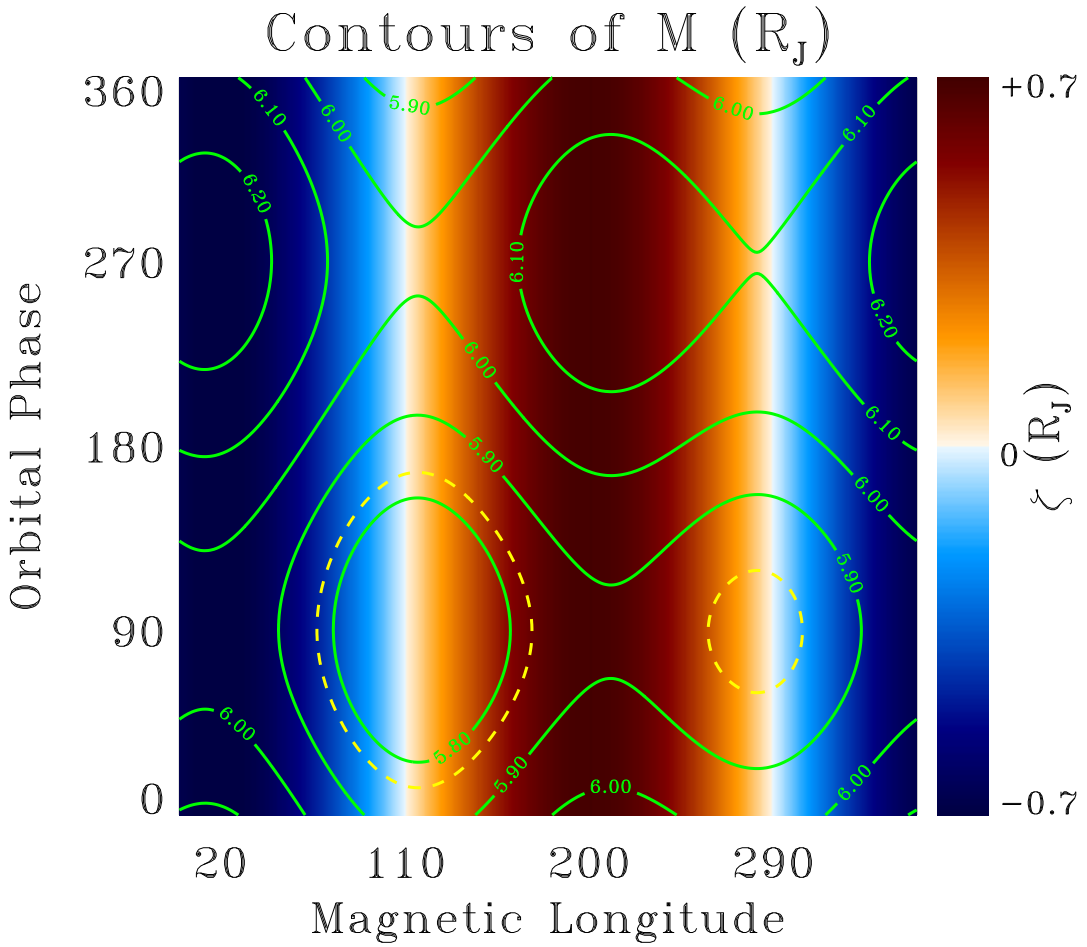


Figure 5.6 Contours of Io's M-value as functions of Io's magnetic and orbital longitudes. The broken yellow circles indicate the location of the ribbon, fixed in this coordinate system at M=5.83 $R_J$. The color indicates Io's $\zeta$ value, with darker color indicating that Io is farther from the centrifugal equator. The color is red when Io is north of the torus and blue when Io is south of the torus.

torus. As discussed above, one effect is to shift the torus dawn-ward. The second effect of the electric field is that a torus ion experiences a changing magnetic field as it is swept around Jupiter. This results in a modulation of both the electron density and temperature proportional to $(L(270°)/L(\phi))^2$ where L($\phi$) is the L-shell of the torus ion at orbital phase $\phi$ and L(270°) is the L-shell of the ion at western elongation (Smyth and Combi 1988b). These authors used a theoretical calculation of this variation based on the inferred strength of the east/west electric field and the expected motion of the plasma through the torus. I use instead observations of the eastern and western ansae of the torus to impose an empirical local time variation in the form:

$$C_{LT} = 1 - A_{LT}\,(1 + \sin\phi) \tag{5.6}$$

where $C_{LT}$ is the local time correction factor as a function of local time ($\phi$) and $A_{LT} = (1 - n_{e,east}/n_{e,west})$ is the amplitude of the variation. The value of $A_{LT}$ is determined from observations of ribbon intensity. Schneider and Trauger (1995) measured an east/west intensity ratio in the ribbon of $I_{east}/I_{west} = 0.86$ (Figure 5.4b). Taking into account line-of-sight brightness effects, the east/west electron density ratio in the centrifugal equator is $n_{e,east}/n_{e,west} = 0.94$, or $A_{LT}$=0.03. An additional measurement of the east/west intensity ratio is given by Brown (1994) who took into account line-of-sight effects when determining the intensity ratio in the warm torus. This measured value is $I_{east}/I_{west} = 0.78$, implying $A_{LT} = 0.04$, consistent with that predicted by Smyth and Combi (1988b) based on the inferred magnitude of the east/west electric field and the assumption that the plasma expands in three dimensions as it moves from west to east.

(2) System-III Variations: The intensity in the plasma torus varies as a function of magnetic longitude (Figure 5.4b). Schneider and Trauger (1995) found that the

intensity in the ribbon varies in the form:

$$I(\lambda) \sim 1 + 0.39 \cos(\lambda - 200^\circ) \tag{5.7}$$

The observations by Brown (1994) were more sensitive to variability in the warm torus and found:

$$I(\lambda) \sim 1 + 0.35 \cos(\lambda - 180^\circ) \tag{5.8}$$

This variation results from a combination of changing electron density and scale height in the torus, as seen in the observations of Schneider and Trauger (1995): when the longitude of the ansa is near 200°, the ribbon is short and bright; at longitudes near 20°, the ribbon is tall and dim. Schneider et al. (1997) suggested that the total flux tube content (the ion column integrated along the field line) may remain constant along a magnetic field line over the period of the magnetic field rotation. The flux tube content can be expressed as:

$$N = \sqrt{\pi} n_0 H \tag{5.9}$$

where $n_0$ is the electron density on the centrifugal equator. $H = \left(\frac{3kT_\parallel}{3m_i\Omega^2}\right)^{1/2} \propto T_\parallel^{1/2}$ is the plasma scale height Hill and Michel (1976). Therefore,

$$n_0 \propto \frac{1}{H} \propto \frac{1}{\sqrt{T_\parallel}} \tag{5.10}$$

This simplification allows the observed System-III variations in the torus to be expressed as a function of a single parameter: the parallel ion temperature. The variation in $\mathrm{T}_\parallel$ is expressed as:

$$T_\parallel(\lambda) = T_0 + A_{T_\parallel} \cos\left(\lambda - \lambda_{T_\parallel}\right) \tag{5.11}$$

where $\mathrm{T}_0$ is the average ion temperature, $\mathrm{A}_{T_\parallel}$ is the amplitude of the variation, and $\lambda_{T_\parallel}$ is the longitude of maximum temperature. Based on modeling of the images in Schneider and Trauger (1995), Schneider [personal communication]

found that $T_0 = 17.4$ eV, $A_{T_\parallel} = 8.5$ eV, and $\lambda_{T_\parallel} = 46°$ in the ribbon (Figure 5.4c), and $T_0 = 74.8$ eV, $A_{T_\parallel} = 15$ eV, and $\lambda_{T_\parallel} = 22°$ in the warm torus. The scale height and electron density can then be expressed as functions solely of the parallel ion temperature:

$$\begin{aligned} H\left(T_\parallel\right) &= H\left(T_0\right)\sqrt{\frac{T_\parallel}{T_0}} \\ n\left(T_\parallel\right) &= n\left(T_0\right)\sqrt{\frac{T_0}{T_\parallel}} \end{aligned} \tag{5.12}$$

The intensity variations observed by Schneider and Trauger (1995) and Brown (1994) can be simulated with the ribbon temperature results above. The warm torus temperature results produce a lower amplitude variation in the temperature.

Combining these modulations, the electron density and temperature in the torus as functions of M, $\zeta$, $\phi$, and $\lambda$ are given by:

$$\begin{aligned} n_e\left(M,\zeta,\phi,\lambda\right) &= n_{e,west}(M)e^{-\left(\zeta/H(T_\parallel(\lambda))\right)^2}C_{LT}(\phi)\sqrt{\frac{T_0}{T_\parallel(\lambda)}} \\ T_e\left(M,\zeta,\phi,\lambda\right) &= T_{e,west}(M)C_{LT}(\phi) \\ n_i\left(M,\zeta,\phi,\lambda\right) &= n_{i,west}(M)e^{-\left(\zeta/H(T_\parallel(\lambda))\right)^2}C_{LT}(\phi)\sqrt{\frac{T_0}{T_\parallel(\lambda)}} \end{aligned} \tag{5.13}$$

where $n_{e,west}(M)$, $T_{e,west}(M)$, and $n_{i,west}$ are the electron density, electron temperature, and ion density, respectively at western elongation measured by Voyager (shown in Figure 5.3) and the exponential factor takes into account the distance along the field line from the packet to the centrifugal equator. The electron temperature along field lines is constant and therefore does not depend on $\zeta$. $C_{LT}$ is given by Equation 5.6; the parallel ion temperature, $T_\parallel$, depends on $\lambda$ according to Equation 5.11.

Combining these idealized variations with the observations referred to above, I have developed a "basic torus" and a "varying torus" which I will take as starting points for studies of Io's corona and extended neutral clouds. The basic torus uses the Voyager

data as its western profile and includes the local time modulation that results from the presence of the east/west electric field. There are no magnetic longitude effects included so that there are no temporal variations in the torus brightness and scale height. The varying torus adds one more layer of complexity by including the System-III variability with the constant flux tube content assumption. In this implementation I use quantities consistent with the observations discussed: the ribbon is offset from the center of Jupiter 0.061 $R_J$ toward $\lambda = 149°$. The value of $\epsilon$ is 0.24 resulting in a shift of the ribbon east 0.14 $R_J$. The radial electron density and temperature profiles used are the Voyager profiles with the following local time and System-III modulations:

$$C_{LT}(\phi) = 1 - 0.03(1 + \sin\phi) \tag{5.14}$$

$$T_{\parallel}(\lambda) = 17.4 + 8.5\cos(\lambda - 46°) \tag{5.15}$$

The temperature variation is based on the ribbon measurements as they do a better job of replicating the observed brightness variations.

The major strength in the treatment of the torus that I have developed is that it takes into account the theoretical and observational evidence of torus variability. Different ways in which the torus has been observed to vary have been included when determining the neutral lifetimes. This treatment has also been designed with future torus observations in mind: both changes in the magnitudes of the modulations already included as well as any new ways in which the torus might be discovered to vary can easily be included. This is essential since the combined published and unpublished observations of the torus do not show a constant, repeatable set of variations. Instead, the magnitude and form of torus variability is itself variable. An ideal study of the instantaneous state of the neutral clouds would include the instantaneous torus state, which, unfortunately, is not always available. My canonical torus is based on the most comprehensive study of torus variability during a single week. I assume that it is representative of the normal variability. Additionally in the subsequent chapters of this thesis

I impose changes in the torus density and density, the strength of the east/west electric field, and the amplitude of the variations to determine how these different quantities affect the neutrals.

One assumption I have made is that the different regions of the torus do not vary independently. There is no observational or theoretical requirement that the cold torus, ribbon, and warm torus must vary in the same way. To reduce the number of free parameters and make the torus more manageable, there is no radial dependence on the density variations. A more detailed description of the plasma torus can easily be implemented into this neutral cloud model in the future as they become available.

### 5.3.3 Neutral Lifetimes in the Inner Jovian System

Because the atomic properties of oxygen, sulfur, and sodium are different, the processes responsible for their loss from the neutral clouds are different. As discussed in Chapter 2, the two important loss processes are electron impact ionization and charge exchange. Figure 5.7 shows the lifetimes of each neutral due to both processes in the region of interest for modeling neutral clouds. The plasma conditions used to calculate the lifetimes are those measured by Voyager at western elongation Bagenal (1994); no System-III variability is taken into account. From the top panel it can be seen that the lifetime of sodium is dominated completely by electron impact ionization. For modeling purposes, it is only necessary to consider electron impact ionization of sodium and charge exchange is ignored.

The loss of oxygen, on the other hand, is dominated by charge exchange. The dominant reaction, shown by the broken blue line is Figure 5.7(b) is $O + O^+ \rightarrow O^+ + O$. This reaction dominates due to the combination of high cross section for change exchange (Table 2.3) and the high abundance of singly ionized oxygen in the torus.

Sulfur presents a mix of charge exchange and electron impact ionization. In the cold torus, within $\sim$ 5.7 $R_J$, the charge exchange reaction $S + S^+ \rightarrow S^+ + S$

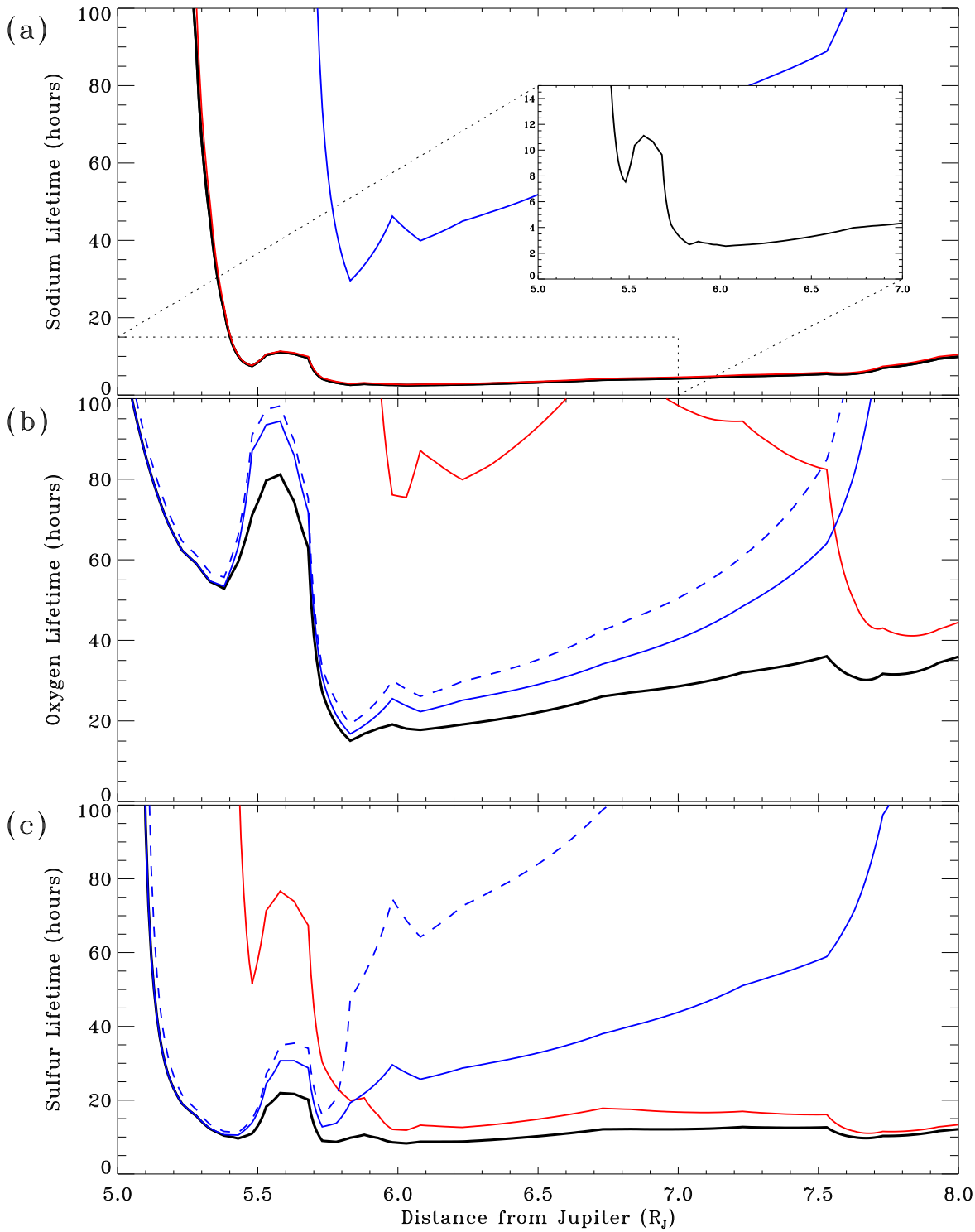


Figure 5.7 Neutral lifetimes in the inner Jovian system for (a) sodium, (b) oxygen, and (c) sulfur due to electron impact ionization and charge exchange. The black lines are the neutral lifetimes, the red lines are the lifetimes if the only active process is electron impact ionization, and the solid blue lines are the lifetimes if only charge exchange is active. The broken blue lines are the lifetimes due to the dominant charge exchange processes (as discussed in the text).

dominates due to the same considerations as the oxygen reaction above. In the ribbon region, the processes undergo a change with electron impact ionization dominating the total ionization in the warm torus. This change takes place because the density of $S^+$ drops off very quickly outside the ribbon, minimizing the importance of charge exchange. Additionally, the change in electron temperature from the cold torus to the warm torus corresponds to a sharp increase in the rate coefficient of sulfur electron impact ionizations (Figure 2.5) maximizing the importance of electron impact ionization. This switch from one ionization process to the other is not likely to have much impact since both the electron and ion densities vary in the same way off the centrifugal plane and have the same local time and magnetic longitude variations.

The offset and tilt of the dipole along with the east/west electric field cause constant changes in the plasma conditions near Io. Add to this the observed torus variability and it becomes clear that the neutral lifetime in Io's corona is a rapidly changing quantity. Figures 5.8 and 5.9 show the changing lifetimes for each species at Io for the basic and varying tori, respectively.

The lifetimes in the basic, longitudinally symmetric torus are much less variable than in a torus which varies with magnetic longitude. This is of course quite reasonable; Io experiences a much wider range of plasma conditions in the variable torus. One basic trend which holds true for both torus models is that the lifetimes of all species are longer at Io's eastern elongation than at Io's western elongation. This provides the most basic explanation for the observed east/west brightness asymmetry in the sodium cloud near Io (Smyth and Combi 1988b) and is investigated in Section 5.4.2.

*Comparison with Smyth and Combi (1988b)*

The most complete modeling study of the neutral clouds prior to this work was that of Smyth and Combi (1988b). Significant differences between that work and the current one exist in the treatment of the plasma torus and the determination of neutral lifetimes. Here I discuss several of the strengths of my treatment of these important

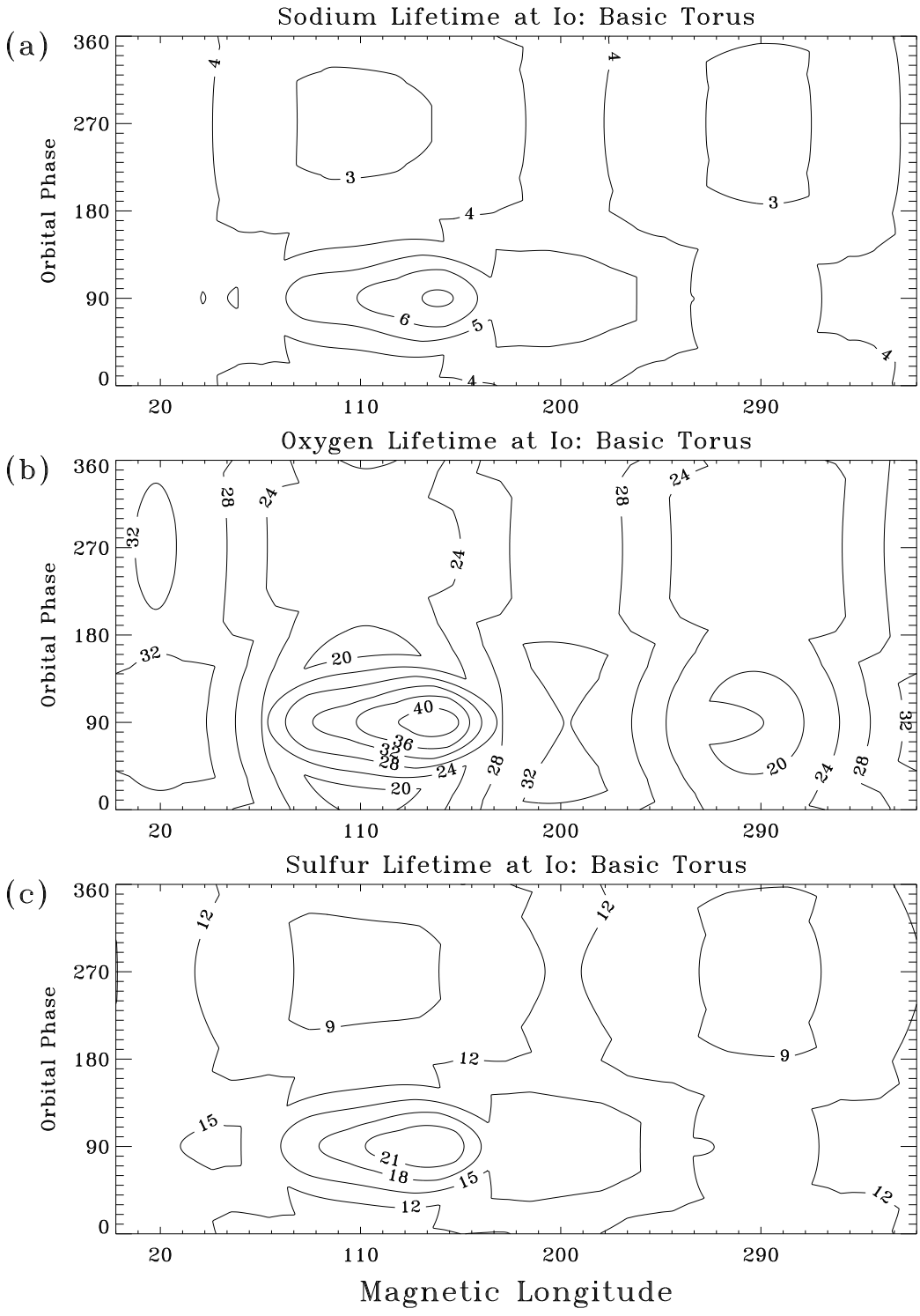


Figure 5.8 Neutral lifetimes in hours for (a) sodium, (b) oxygen, and (c) sulfur at Io as a function of Io's magnetic longitude and local time for a torus which does not vary with magnetic longitude.

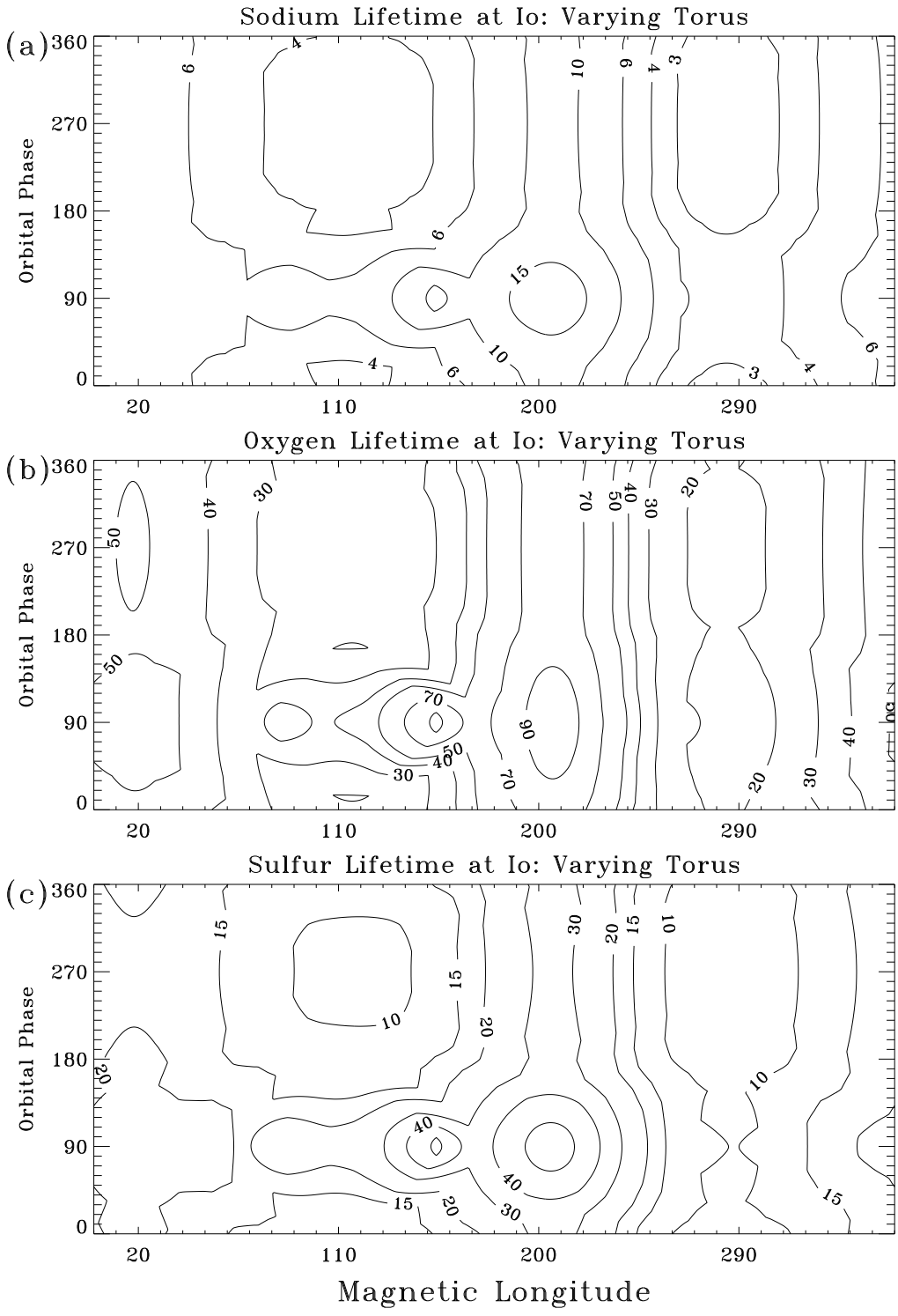


Figure 5.9 Neutral lifetimes in hours for (a) sodium, (b) oxygen, and (c) sulfur at Io as a function of Io's magnetic longitude and local time for a torus which varies with magnetic longitude.

aspects of neutral cloud modeling and contrast it with the previous work.

Two observational results published in recent years have important consequences for the neutral clouds. As discussed in Chapter 2, measurements of the electron impact cross section of neutral sodium (Johnston and Burrow 1995) imply that the sodium lifetime in the torus is $\sim 1.4$ times longer than previously thought. Consequently, the lifetimes predicted by Smyth and Combi (1988b) are too short and their estimates of the sodium source rate are too high.

The observations of Schneider and Trauger (1995) previously discussed point out two ways in which the plasma torus model used by Smyth and Combi is incomplete. First, the observations show that the brightness and scale height in the torus vary with magnetic longitude. This aspect of the torus was not included in their torus treatment, although these variations are not a first order effect on the shapes of the corona and neutral clouds. A more important difference, however, is the observation that the ribbon oscillates with an amplitude approximately half that of the offset of Jupiter's dipole field. This reduces the range of lifetimes that is experienced in Io's corona because a smaller region of the torus is traversed by Io.

Even taking these differences into account, I predict different sodium lifetimes at Io than Smyth and Combi (Figure 5.10). In panel (b), the lifetimes were computed using the coordinate transformation to the plasma torus described in Section 5.3.2 with the difference that the offset of the ribbon from the center of Jupiter is assumed to be 0.12 $R_J$. Additionally, the lifetimes were determined used the older sodium cross sections (Zapesochnyi and Aleksakhin 1969) for consistency with the results of Smyth and Combi which are shown in panel (a). The basic morphologies of the two contour plots in Figure 5.10 are similar: the lifetime is shorter when Io is west of Jupiter than when it is east of Jupiter, and the lifetime extrema occur at approximately the same magnetic longitudes and orbital phases.

The main difference between the two lifetime calculations is the range of lifetimes

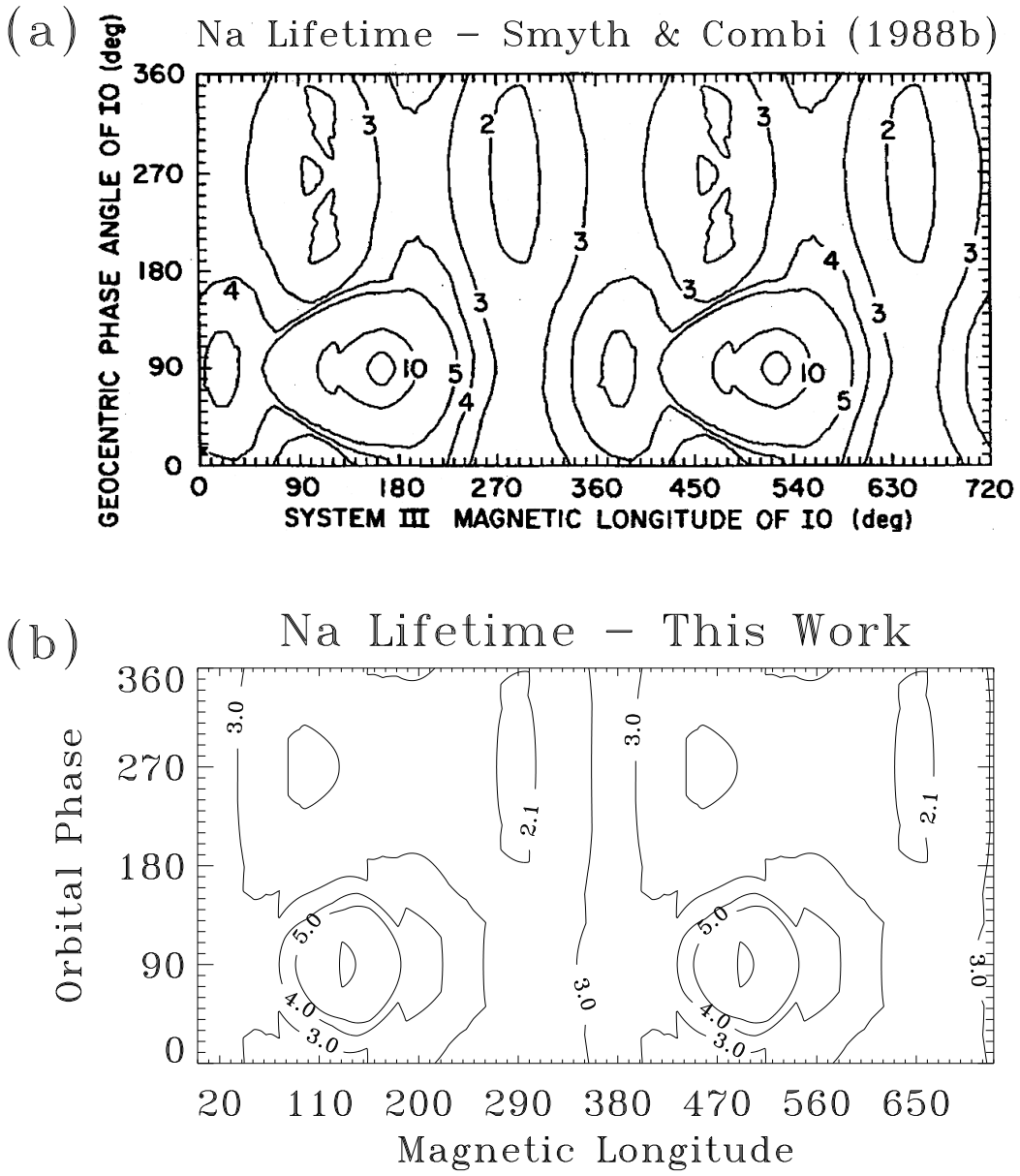


Figure 5.10 Comparison of the sodium lifetime in the corona predicted by (a) Smyth and Combi (1988b) and (b) this work using a similar torus description.

experienced at Io is smaller for my torus parameterization: I calculate a range of 2 to 11 hours compared with Smyth and Combi's range of 2 to 15 hours. This difference arises from differences in the nature of the transformation to the plasma torus coordinate system. Because the torus is aligned along the centrifugal equator, it is always parallel to Jupiter's rotational axis (Figure 5.2). Smyth and Combi, however, assume a torus that is tilted 7° relative to Io's orbital plane. My transformation assumes that the dipole is tilted relative to the plane and the torus is aligned along the centrifugal equator, but extended parallel to the rotation axis which is not perpendicular to the centrifugal equator.

### 5.3.4 Flux Distributions

The major physical processes which results in neutral ejection from Io's exobase is sputtering as discussed in Chapter 2. The parameter $v_b$ is chosen to give the desired most probable velocity $v_p$. In the discussion in this chapter and the following chapters, the parameters $v_p$ and $\alpha$ are varied to change the sputtering distribution.

In addition, a general exponential distribution is used as a means to test other speed distributions. This distribution is in the form:

$$f(v) \propto v^{\beta} e^{-(v/v_T)^2}, \; v_T = \left(\frac{2kT}{m}\right)^{1/2} \tag{5.16}$$

$\beta = 3$ corresponds to a Maxwell-Boltzmann velocity distribution and $\beta = 5$ corresponds to Jeans escape.

An important consideration when discussing atmospheric escape is that escape from the exobase does not imply escape from Io. For most of the speed distributions which will be discussed in later chapters, the most probable speeds are less than Io's escape velocity from the exobase. This implies that, barring ionization in the corona, most atoms will re-impact the surface. Figure 5.11 gives the fraction of the speed distribution with velocity greater than 2.1 km $s^{-1}$, the escape velocity from Io's exobase.

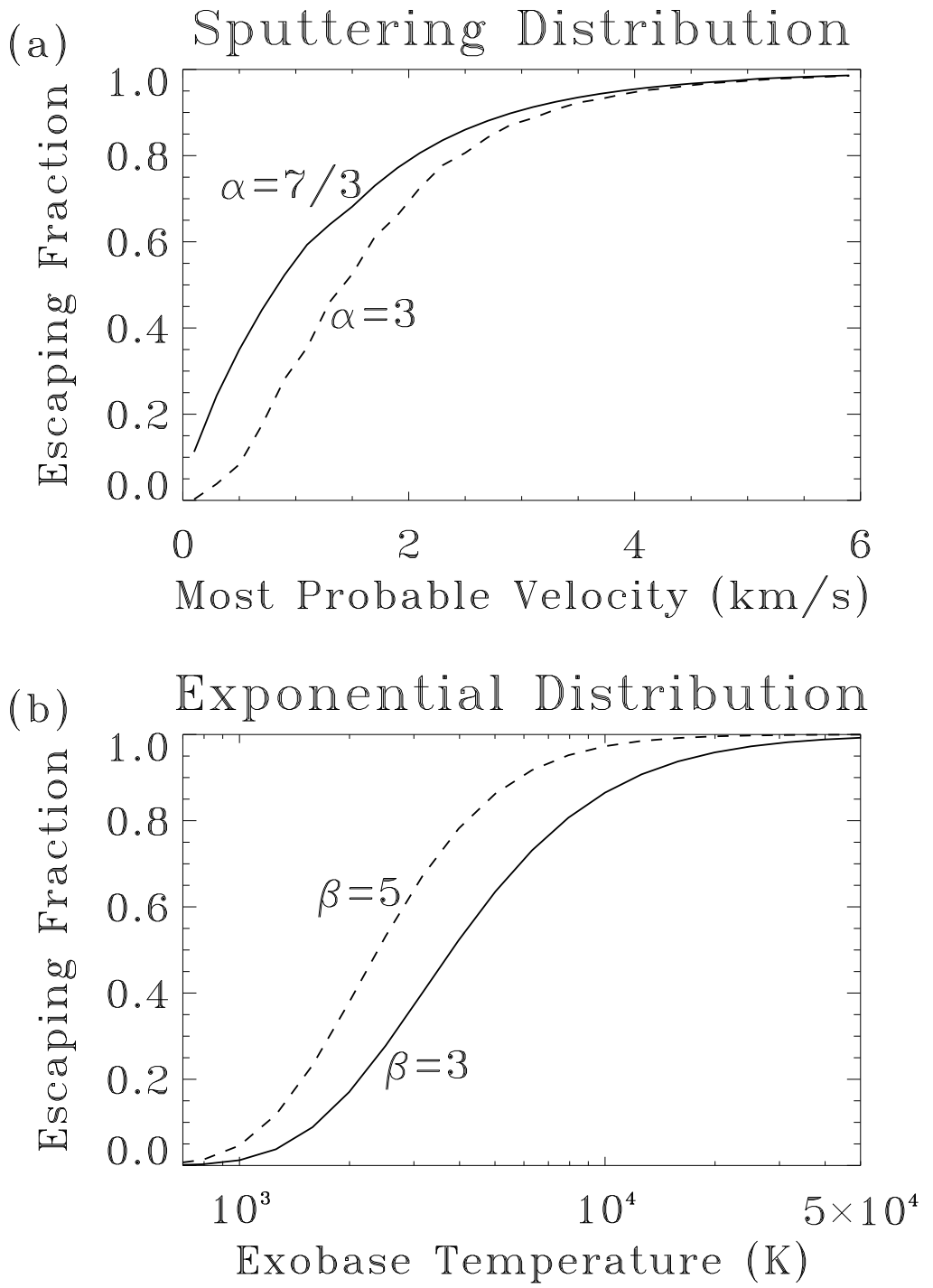


Figure 5.11 (a) Fraction of the atoms escaping from the exobase in a sputtering speed distribution with escape velocity as a function of most probable speed. (b) Same as (a) with an exponential speed distribution from the exobase.

The escaping source rate can be determined from these curves for a stated exobase source rate. For example, with a sputtering distribution with $\alpha = 3$ and $v_p = 0.7$ km s$^{-1}$, 20% of the ejected atoms have escape velocity. The actual percentage of these atoms that escape will depend on the neutral lifetime in the corona.

## 5.4 Basic Tests of the Neutral Cloud model

In this section I present several basic tests and characteristics of the neutral cloud model. I first discuss the effect of radiation pressure on the sodium agreeing with Smyth and Combi (1988b) who concluded that the effect is small compared to other factors which affect the changing cloud morphology and is not important for defining the large scale sodium cloud morphology. I also use the model to reproduce two previously observed asymmetries in the sodium cloud: the east/west brightness asymmetry (Bergstralh et al. 1975, 1977) and the north/south brightness asymmetry (Trafton and Macy 1975).

### 5.4.1 Effect of Radiation Pressure

Previous modelers (Smyth 1979, 1983) have determined that the effects of radiation pressure result in an asymmetry between Io's brightness at eastern and western elongation qualitatively similar to that observed by Bergstralh et al. (1975, 1977). Since then, Smyth and Combi (1988b) showed that radiation pressure is a second order effect; the effect of the plasma torus on the east/west asymmetry is more important than radiation pressure. Figure 5.12 demonstrates the effect of radiation pressure on the extended cloud and the corona. In both the large field of view showing the inner Jovian system and the smaller views focusing on Io's corona, changes in the streamlines point to perturbations caused by incident solar photons. However, this effect would be hard to observe due to several considerations. In the corona (Figure 5.12(b)-(c)), radiation pressure "pushes" the corona slightly away from the sun: streamlines of atoms ejected

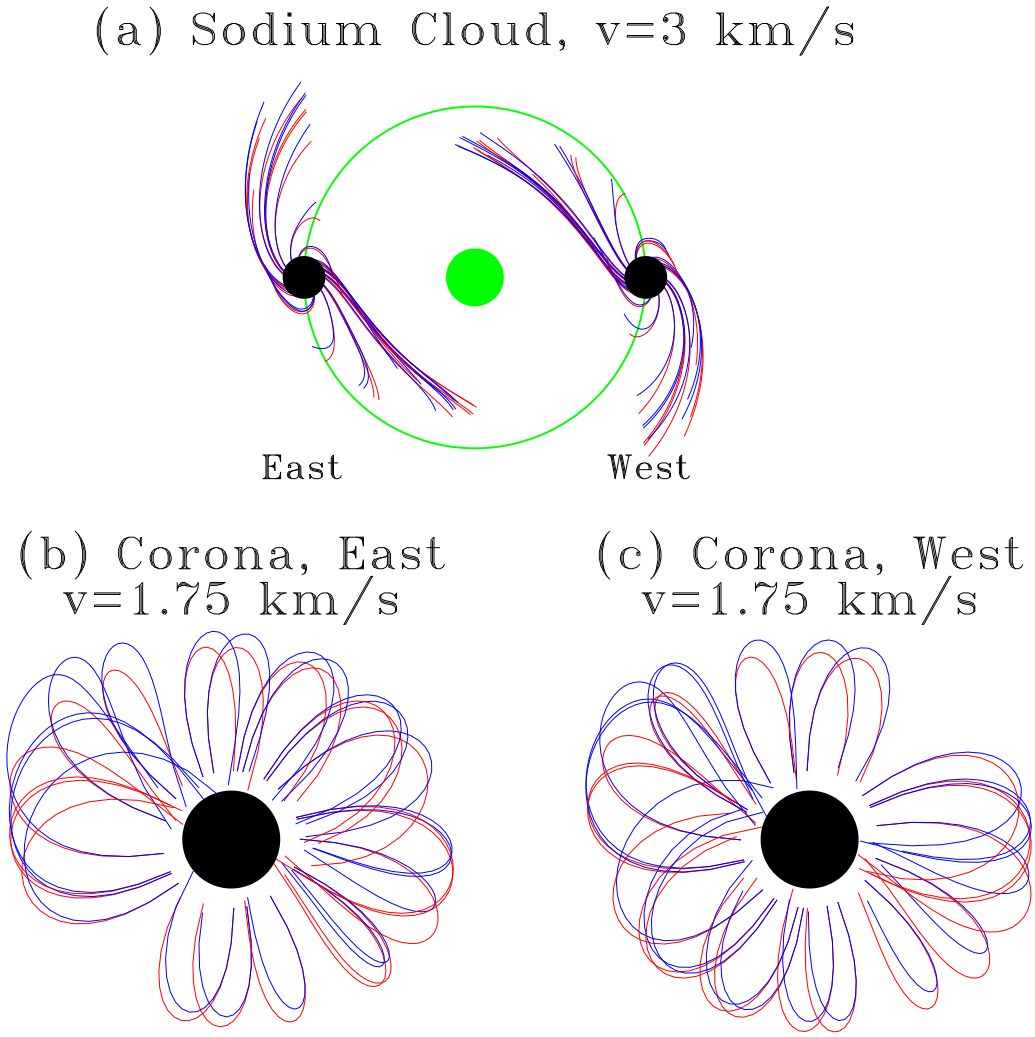


Figure 5.12 Effect of radiation pressure on neutral sodium atoms in the cloud and corona. The top panel shows twenty hours streamlines of sodium ejected from Io at eastern and western elongation with a velocity of 3 km $s^{-1}$. The red streamlines show the motion of sodium when radiation pressure is not included; blue streamlines include radiation pressure. The bottom panels show the corona at eastern and western elongation for particles ejected radially with velocity=1.75 km $s^{-1}$

toward the sun are slightly compressed and those of atoms ejected away from the sun are slightly elongated. However, there is no east/west effects, so the column density in the corona along the line of sight would not change. In the cloud (Figure 5.12(a)), the effects of ionization by the torus dominate over changes in the trajectories of neutrals (see Chapter 7). The time scale for observable changes due to radiation pressure is greater than the lifetime of the sodium atoms.

### 5.4.2 Testing the model: East/West Sodium Brightness Asymmetry

In order to demonstrate that the current model can describe the earliest observations of the sodium cloud, I present modeled examples of two asymmetries observed in the sodium emission. The first is the east/west brightness asymmetry reported by Bergstralh et al. (1977). This study found that the sodium cloud is $\sim 25\%$ brighter at eastern elongation than at western elongation. This difference is not due to radial velocity differences since at elongation the radial velocities are equal in magnitude. The study did correct for Jupiter's radial velocity relative to the sun.

Smyth and Combi (1988b) looked at the effects on sodium lifetime of the Io plasma torus and the east/west electric field which shifts the torus dawn-ward. As can be seen in Figures 5.8 and 5.9, the lifetime of sodium is longer near eastern elongation than western elongation. Since less sodium is ionized east of Jupiter, the density, and subsequently the brightness, is greater. This is demonstrated in Figure 5.13 which shows modeled examples of the east/west asymmetry. The top panel shows the sodium brightness as a function of orbital phase modeled for a single sputtering distribution. The dominant factor on the shape of this curve is the changing value of $\gamma$ and is discussed in greater detail in Chapter 7. When local time variations in the torus caused by the east/west electric field are not taken into account, the ratio of brightness at $\phi = 90^\circ$ to the brightness at $\phi = 270^\circ$ is $\sim 1$ (a small deviation from unity results from the slight asymmetry in the $D_2$ Fraunhofer line). In Figure 5.13, this ratio is $\sim 1.22$ and

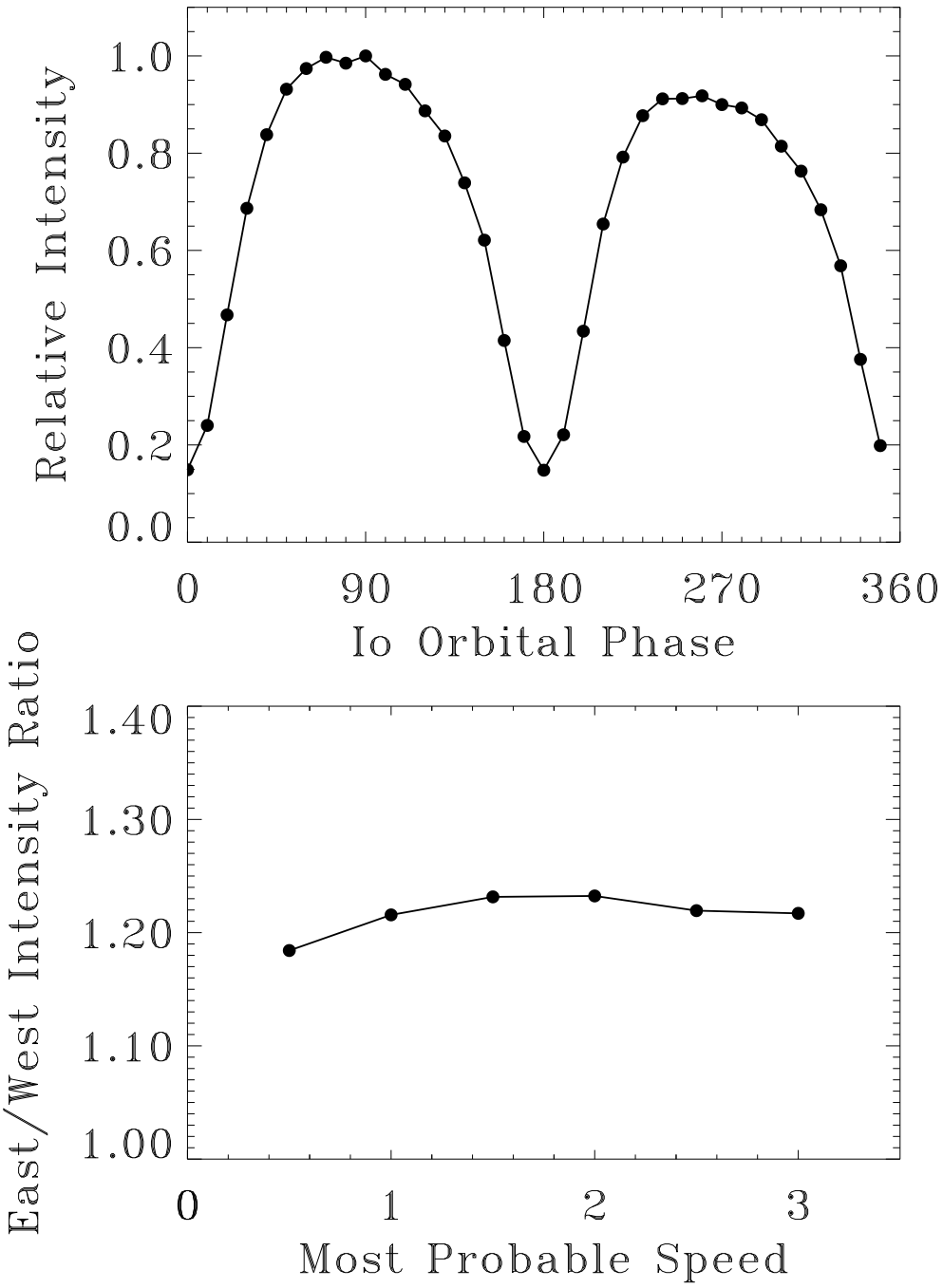


Figure 5.13 Demonstration that the current model reproduces the observed east/west brightness asymmetry in the sodium cloud. (a) The top panel shows the brightness of the sodium cloud as a function of orbital phase for a sputtering distribution with $\alpha = 3$ and $v_p = 3.0$ km s$^{-1}$. (b) Modeled east/west brightness ratio as a function of the most probable speed of the sputtering distribution.

does not vary greatly with most probable speed of the sputtering distribution. The only difference is that the lifetime of sodium near Io is longer on Jupiter's dawn side than on the dusk side so sodium in the corona close to Io is not lost as quickly. The effect of the east/west electric field on the corona is discussed further in Chapter 6.

### 5.4.3 Testing the model: North/South Sodium Brightness Asymmetry

A second type of asymmetry was discovered in the sodium cloud at about the same time as the first. This is an asymmetry in the spatial distribution of the sodium near Io and is related to the interaction of the neutrals with the plasma torus. Spectra taken by Trafton and Macy (1975) 7.5", 15", and 30" north and south of Io show a correlation between north/south brightness ratio and Io's magnetic latitude. When Io is south of the magnetic equator, the cloud is brighter south of Io than north; similarly, when the cloud north of Io is brighter when Io is north of the magnetic equator. This result was confirmed by Trafton (1977); Trafton and Macy (1977) and Murcray and Goody (1978), the latter of whom examined images of the sodium cloud to detect this asymmetry.

An explanation for this asymmetry came with the discovery of the plasma torus: the neutral lifetime is shorter on the side of Io closer to the centrifugal equator, so the sodium intensity on that side is less (Trafton 1980). This hypothesis can be tested by using the neutral cloud model (Figure 5.14) to simulate images of the sodium cloud at a range of magnetic longitudes. The quantity $(I_N - I_S)/(I_N + I_S)$ was suggested by Murcray and Goody (1978) as a way of removing any calibration differences between their data and Trafton's data. Fits to the two data sets (computed by Murcray and Goody (1978)) are shown over model calculations of the asymmetry 15" north and south of Io. As can be seen, the model successfully predicts a north/south asymmetry that is qualitatively similar to that observed.

The 1980 paper by Trafton suggested that the plasma torus is the source of the

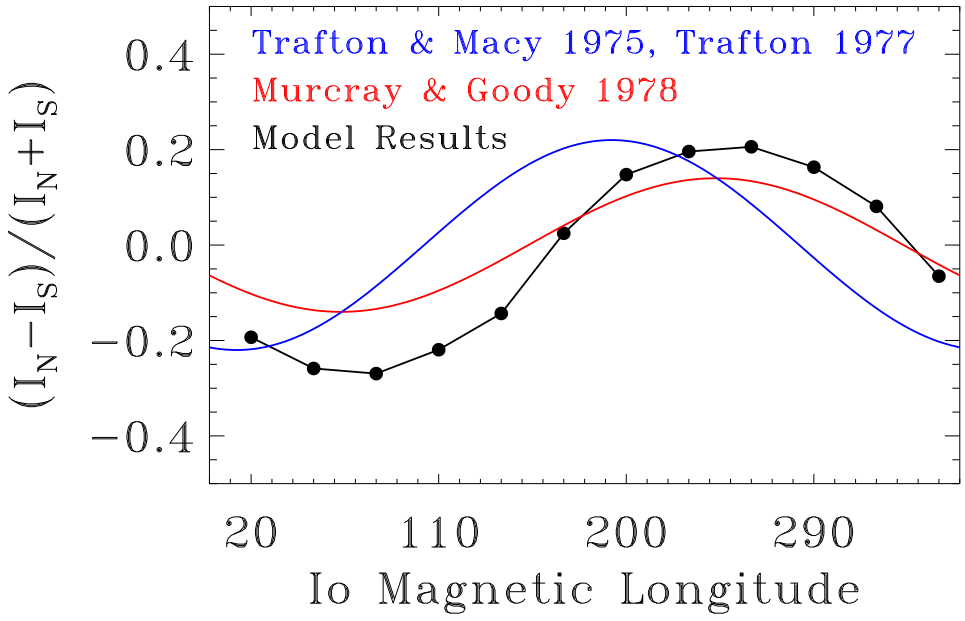


Figure 5.14 Demonstration of the north/south asymmetry in the sodium cloud observed by Trafton and Macy (1975).

north/south asymmetry, but this is the first modeling effort which attempts to explain these observations. There has been comparatively little interest in the north/south sodium brightness ratio, although it is a potential measure of the torus scale height. A comparison of the sodium densities at two points on opposite sides of Io indicates a difference in the neutral lifetimes and the electron densities, which can lead to the scale height in the torus.

## 5.5 Summary

A model has been developed to study Io's corona and extended neutral clouds. It is an extension of the model of Wilson and Schneider (1999) who have used it to study solar system sodium in all its glory including Io's fast sodium features (the directional feature and molecular ion stream), the extended sodium disk around Jupiter, and the lunar sodium tail. The model calculates the paths of neutral atoms under the influence of gravity and radiation pressure from Io's exobase to their loss by electron-impact ionization, charge exchange, or collision with Io or Jupiter.

The main contributions I have made to this model are the treatment of the Io plasma torus and the calculation of neutral lifetimes. Using observations of the plasma torus (Bagenal 1994; Schneider and Trauger 1995; Brown 1994), I have parameterized several features of the motions and variability the torus is observed to exhibit. Jupiter's dipole axis is tilted relative to its rotational axis; the plasma torus is lies along the centrifugal equator, but is oriented parallel to the rotational axis. The dipole offset produces an oscillation of the torus relative to Jupiter: the ribbon is observed to move back and forth with an amplitude of 0.6 $R_J$. An additional effect on the position of the torus is caused by the dawn to dusk electric field across the Jovian system. This electric field perturbs the orbits of torus ions such that the entire torus is shifted dawnward. One observational consequence of this shift is that the ribbon feature in the torus appears closer to Jupiter at the western ansa than the eastern asna.

Observations of the torus have detected variations in the torus intensity as function of both local time and magnetic longitude. The local time variations are a consequence of the east/west electric field Barbosa and Kivelson (1983); Ip and Goertz (1983). The origin of the magnetic longitude variations is not understood, but the observations suggest that the flux tube content along field lines remain constant (Schneider et al. 1997) which simplifies the problem of parameterizing the plasma properties.

I have developed a method for determining the local plasma densities and temperatures for each packet in the model simulations as a function of its location relative to Jupiter and magnetic longitude. The description of the torus includes the effects of the offset tilted dipole, the east/west electric field, and the observed System-III variability. The nominal densities and temperatures of the plasma that are used are the measurements from the Voyager flybys of Jupiter determined by Bagenal (1994). The magnitude of each of deviation from the average state of the torus is based on ground-based observations of the torus (Schneider and Trauger 1995; Brown 1994).

By using the empirical torus parameterization, I have determined the lifetimes of neutral sodium, oxygen, and sulfur in the inner-Jovian system and compared the relative importance of electron-impact ionization and charge exchange for each species. I also compared the current calculation of the sodium lifetime with a previous result by Smyth and Combi (1988b). Although the main differences between the two lifetime calculations result from recent measurements of the sodium electron impact cross section (Johnston and Burrow 1995) and the observations that the amplitude of torus oscillation is only half the magnitude of the dipole offset, Smyth and Combi (1988b) used a torus that is perpendicular to the centrifugal equator rather than the Jupiter's orbital plane.

The chapter concluded with several applications of the model to Io's neutral clouds. First, I demonstrated the effects of radiation pressure previously described by Smyth (1983) and concluded that they are insignificant compared with the larger effects of ionization by the plasma torus. Next, I simulated the east/west brightness asymmetry

measured by Bergstralh et al. (1975, 1977) and confirmed the model results of Smyth and Combi (1988b) which determined that the asymmetry is a result of the effect of the east/west electric field on neutral lifetimes. Lastly, I demonstrated that the magnetic longitude dependence on the ratio of sodium brightness north of Io to the brightness south of Io (Trafton and Macy 1975) is a consequence of non-uniform ionization by the plasma torus as predicted by Trafton (1980).